Insight Into The X-Ray Absorption Spectra of Cu-Porphyrazines From Electronic Structure Theory

Esma Birsen Boydas,[†] Bernd Winter,[‡] David Batchelor,[*,¶] and Michael Roemelt[*,†]

†*Lehrstuhl für Theoretische Chemie, Ruhr-Universität Bochum, D-44780 Bochum, Germany*

‡ *Fritz-Haber-Institut der Max-Planck-Gesellschaft, Faradayweg 4-6, D-14195 Berlin,Germany*

¶*Karlsruher Institut für Technologie, Institut für Synchrotron Strahlung, 76021 Karlsruhe, Germany*

E-mail: david.batchelor@kit.edu; michael.roemelt@theochem.rub.de

Abstract

Transition metal porphyrazines are a widely used class of compounds with applications in catalysis, organic solar cells, photodynamic therapy and nonlinear optics. The most prominent members of that family of compounds are metallophtalocyanines that have been subject of numerous spectroscopic and theoretical studies. In this work, the electronic structure and X-ray absorption characteristics of three Cu-porphyrazine derivatives are investigated by means of modern electronic structure theory. More precisely, the experimentally observed N K-edge and Cu L-edge features are presented and reproduced by time-dependent density functional theory, restricted open-shell configuration interaction and a restricted active space approach. Where possible, the calculations

are used to interpret the observed spectroscopic features in terms of electronic transitions and furthermore connect spectral differences to chemical variations. Part of the discussion of the computational results concerns the impact of various parameters and approximations that enter the calculations, e.g. the choice of active space.

Introduction

X-ray absorption spectroscopy (XAS) is a powerful inner-shell spectroscopic technique that is able to probe the electronic structure of molecules and solids alike. During the experiment an electron from an inner shell is promoted to the valence shell or the continuum. Hence the energy range for the required X-ray beam is governed by both, the specific element and the inner shell that the electron originates from. Consequently all experimentally observed features are labeled according to these two parameters. For example, the absorption bands that mainly correspond to transitions from the 1s shell of a Cu atom are referred to as Cu K-edges. Owing to its element specificity XAS is particularly well suited to investigate the local electronic properties of transition metals even in large ligand environments such as metalloproteins. Depending on the used experimental technique different properties are accessible including the metal oxidation state, electronic configuration, spin symmetry, the ligand environment and metal-ligand bond covalency. However, it has been found recently that an immediate interpretation of absorption data (i.e. total absorption yields) might be problematic in which case it is advisable to rely on various types of partial-yield spectra.[1]

Ligand K-edge features correspond to ligand 1s to np electric-dipole allowed transitions whose intensity mainly maps the ligand p-orbital character in partially occupied and unoccupied molecular orbitals. Consequently the ligand K-edge intensity is widely acknowledged as a measure of metal-ligand covalency.[2–4] Nowadays the interpretation and quantitative analysis of ligand K-edge spectra can be efficiently assisted by quantum chemical calculations. More precisely, the calculation of ligand K-edge features with time-dependent density func-

tional theory (TD-DFT) allows for a relatively simple and straightforward means to assign experimentally observed features to electronic transitions.[4,5]

Experimentally, much sharper and richer features are detected for transition metal L-edges that correspond to dipole-allowed 2p to valence transitions. However, the interpretation of these spectra is significantly more difficult since the manifold of target states features not only 2 open shells – one on the 2p shell and one in the valence shell – but is also subject to strong 2p spin-orbit coupling effects due to the 2p core hole. Accordingly any attempt to model transition metal L-edges in the framework of simple particle-hole models (like TD-DFT) is deemed to fail to reproduce the many occuring multiplets of states and their nontrivial couplings except for a few simple cases. Over the years a number of alternative approaches have been developed that explicitly take into account the multiplet structure of the target states state manifold.[6–12] One of them is the combination of density functional theory with restricted open shell configuration interaction with single excitations (DFT/ROCIS) introduced by Neese *et. al.* It has been shown to yield reasonable results for a variety of different transition metal compounds even for solids.[12–18] Perhaps the most rigorous approach to the problem is based on the restricted active space configuration interaction (RASCI) Ansatz.[19–27] Within this approach the set of molecular orbitals is divided into the internal orbitals that are doubly occupied, the virtual orbitals that are empty and finally two sets of active orbitals that are allowed to have a more involved occupation pattern. The first set of active orbitals comprises the transition metal 2p orbitals from which a single electron is promoted into the second set of active orbitals that correspond to a selection of valence orbitals. A predefined number of states with varying multiplicity is then calculated as a linear combination of all possible configuration state functions (or determinants) within the active space with the correct number of electrons and the desired spin symmetry. The required expansion coefficients are obtained from solving a secular equation that results from minimization of the state energies according to the variational principle. Afterwards spin-

orbit coupling between the different multiplets is accounted for in a Russell-Saunders type fashion. It has been found, however, that accurate results are only achieved when dynamic electron correlation is taken into account.[27]

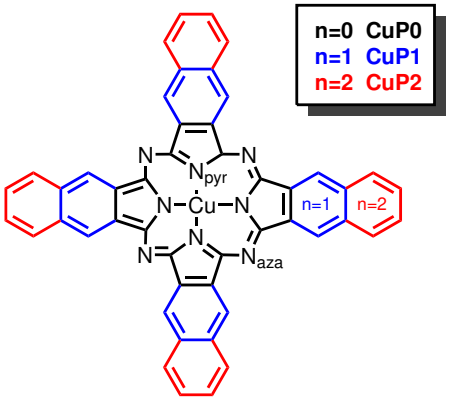

Scheme 1: Copper porphyrazine derivatives CuP0-CuP2 investigated in this work. The nomenclature follows previous works on structurally similar compounds.[28]

In this work, the electronic structure and X-ray absorption characteristics of Cu(II)-porphyrazine scaffolds are investigated. Porphyrazines, or tetraazaporphyrins (usually abbreviated as Pz or TAP), consist of two pyrrole based groups linked together via a meso-tetraaza substitution. Phthalocyanines (Pc's) are porphyrazine analogues consisting of 18 pi-electrons, with four benzo units fused to the pyrrole moieties (see Scheme 1). Metallophthalocyanines (MPc's) belong to one of the most widely investigated macrocycles, due to their chemical value in catalysis, organic solar cells, photodynamic therapy and nonlinear optics.[29–32] Much less investigated, albeit equally prominent derivatives of porphyrazines are napthalocyanines (Nc) with a benzolation degree of 2. The studied set of molecules presents a rare opportunity to study spectroscopic effects of a controlled and systematic variation of the ligand π-system in a transition metal compound. In the following the experimentally observed N K-edge and Cu L-edge features of the three Cu porphyrazine derivatives shown in Scheme 1 will be presented and then simulated by quantum chemical calculations. Where possible, the calculations are used to interpret the observed spectroscopic features in terms

of electronic transitions and furthermore connect spectral differences to chemical variations and their concomitant changes on the local electronic structure at the Cu and N atoms. Part of the discussion of the computational results concerns the impact of various parameters and approximations that enter the calculations, e.g. the choice of active space.

Experimental Details

NEXAFS measurements of the Cu porphyrazines depicted in Scheme 1 were made at BESSYII.[28,33,34] The samples were prepared by *in situ* sublimation on to thin polycrystalline gold films supported on mica substrates. The preparation and initial measurements were carried out in a UHV vacuum chamber on the Dipole magnet Plane grating Monochromator (PGM) beamline PM3. Nitrogen K edge NEXAFS was measured using Auger electron excitation. The thickness was estimated as cirka 80 nm based on calibration using attenuation of Au 4f photoemission. The spot size was of the order of a 1mm to avoid beam damage and so also averaged over any grains present (spectra from different spots showed negligible variation). No charging was observed in the porphyrazine valence or core level photoemission supporting a relatively thin deposited film. A short angular (light incidence angle) investigation showed no intensity variation of the NEXAFS peaks indicating absence of orientational ordering preference in the growth of the films. This is attributed to a rapid growth rate, polycrystalline substrate, and the *tert*-butyl alkyl substituents to the benzene group, hindering π–stacking interaction of the molecules. Comparison of NEXAFS repeat scans on different spots and times showed homogeneously grown films and absence of beam damage. Similarly the photoemission indicated no damage. The samples were transferred to the Cottbusser BTUC Undulator PGM beamline[35] where they were subsequently measured using a low energy resolution Fluorescence detector (EDX) to compare surface and bulk information. Here the Nitrogen edge measurements evidenced a small pre-edge dip due to self absorption

which could simply be corrected for.[36] Both raw and corrected Nitrogen NEXAFS showed the same structure as the data taken at the dipole beamline PM3. The higher photon energy Copper $L_{2,3}$ NEXAFS showed no self absorbtion problem due to the much higher attenuation length of these photons. A small beam damage was observed after several scans for the much higher flux density undulator beamline. In all shown measurements the resolution of the spectra were limited by the sample and not beamline (Undulator PGM resolving power of $\frac{E}{\Delta E} \rightarrow 10000$).

Computational Methodology

In this work multiple sets of calculations on different levels of theory were conducted the majority of which used the ORCA program package in its version 4.2.[37] Geometry optimizations were performed utilizing the global hybrid B3LYP density functional along with def2-TZVP(-f) basis set.[38–40] Accuracy in numerical integration was ensured by a dense grid (ORCA Grid5). The generation of Coulomb and exchange integrals was accelerated with the resolution of identity (RI) and chain-of-spheres (COSX) approximations[41] together with def2/J basis set.[42–45]

Nitrogen K-edge XAS pre-edges were modeled by time-dependent density functional theory (TD-DFT)[46] calculations where electrons were only allowed to be excited from molecular orbitals with predominant ($> 99\%$) N 1s character. Since the core-hole created by the X-ray radiation is localized on a single atom, the N 1s orbitals were localized according to the Pipek-Mezey scheme to truly mimic the underlying phenomena.[47] During all TD-DFT calculations the Tamm-Dancoff approximation is used as implemented in the ORCA program package.[5,48] Scalar relativistic effects were approximated by means of the zeroth order regular approximation (ZORA).[49,50] Calculated spectra were obtained by convoluting the calculated transitions with Gaussian functions with a width of 2.0 eV. Finally, all calculated spectra

are shifted by approximately 12 eV to allow for a better comparison with the experimental analogues. This shift is necessary to account for the systematic errors introduced by the TDDFT approach and depends on the chosen functional and basis set.[51]

The presented calculations of Cu L-edge spectra by means of the above mentioned restricted active space approach included a sequence of different steps. First, the valence active space was selected as described below with the help of the recently introduced ASS1ST scheme that is implemented in the MOLBLOCK program.[52,53] Then all molecular orbitals were optimized with respect to a large number of valence excited states (up to 12 eV) as suggested previously.[25] In the following the conventional (m,n) notation for active spaces will be adopted where m is the number of active electrons and n is the number of active orbitals. After the orbital optimization procedure the Cu 2p orbitals were appended to the active space to provide a final active space that allows for the evaluation of core excited state calculations with a ($2p^5$)(valence^{N+1}) configuration on the RASCI(m,n) level of theory. Importantly, the K calculated RASCI states were divided into ${}^2K$ states with a total spin of $S = \frac{1}{2}$ and ${}^4K$ states with $S = \frac{3}{2}$. The latter set needs to be taken into account because the 2p-to-valence excitation potentially leads to two additional unpaired electrons compared to the electronic ground state. All $K = {}^2K + {}^4K$ state energies were then refined by taking into account dynamic electron correlation effects with second order n-electron valence perturbation theory (NEVPT2) in its strongly contracted variant.[54,55] Finally, spin-orbit coupling (SOC) effects were modeled in the framework of quasi-degenerate perturbation theory which can be regarded as a molecular equivalent to atomic Russell-Saunders coupling.[12] The widely used spin-orbit mean-field (SOMF) approximation was employed during the evaluation of SOC matrix elements.[56] All steps involved in the Cu L-edge spectra calculations used the second-order Douglas-Kroll Hess (DKH2) correction to include scalar relativistic effects.[40,57,58] Accordingly, the cc-pVTZ-DK basis set was chosen.[59–61] Two-electron integrals were evaluating using the RI approximation together with an automatically generated

auxiliary basis set.[62]

Results and discussion

Electronic ground state of CuP0-CuP2

The porphyrazine structures investigated herein adopt a square-planar geometry with a D_{4h} point group symmetry. As shown in Scheme 1 the central Cu ions are coordinated by four pyrrolic nitrogen atoms. The four pyrrole units are connected to a single tetradentate ligand by four additional nitrogen atoms in *meso* position. Consequently two non-equivalent sets of nitrogen atoms labeled N_{pyr} and N_{aza} can be distinguished (see Figure 1). The nomenclature of non-equivalent nitrogens has been adapted from a previous theoretical study on metal-phthalocyanines.[63] Further information on critical bond distances of Cu-N_{pyr} and N_{aza}-C is included in Supporting Information.

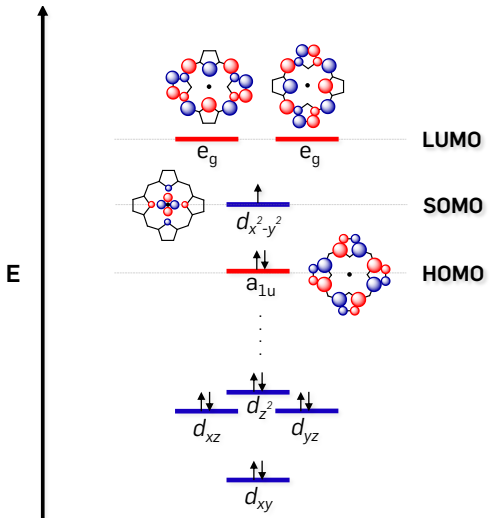

Figure 1: Schematic representation of orbital energy levels for Cu porphyrazine derivatives taking into account the Cu 3d shell and the ligand-centered frontier orbitals. Blue bars are used for orbitals with predominant metal d character while red bars indicate mostly ligand-centered orbitals.

The tetragonal ligand field imposed by the porphyrazine ligand causes a splitting of the

Cu d-orbital energies as shown in Figure 1. In line with previous works on the structurally related phtalocyanines, we find that the molecular orbital corresponding to the Cu $3d_{x^2-y^2}$ orbital lies considerably higher in energy compared to the rest of the Cu 3d orbitals on account of the strong interactions with all four coordinating N atoms.[64] In agreement with the oxidation state of II on the central Cu atom this orbital is only singly occupied in the leading configuration of our CASSCF(7,7) calculations (see below) of the ground state of CuP0 - CuP2. Hence the electronic ground state for all cases is dominated by a Cu ($3d^9$) configuration and therefore exhibits $^2B_{1g}$ symmetry. As expected, the first two unoccupied orbitals are a pair of degenerate π^* orbitals that resemble unoccupied part of the so-called *Gouterman-orbitals* of metalloporphyrins.[65] In contrast to the Gouterman 4-orbital model, however, the pair of ligand centered π orbitals that correspond to HOMO and HOMO-1 in the present cases lose their degeneracy when the macrocycle is endowed with a central metal ion.

Nitrogen K-edge XAS

A comparison of experimental and calculated XAS spectra of N 1s core excitations for all three investigated molecules is given in Figure 2. The oscillator strengths of each calculated transition are represented by sticks which provides additional insight into the peak structures. In general, good agreement between the calculated and experimental spectra is observed in the sense that all significant features in the N 1s-to-π^* region are reproduced well in terms of position and intensity. In all three cases the most intense peak at about 399 eV, labeled as A, gains its intensity from four main transitions. Going from CuP0 to CuP2, the energy splitting between these transitions increases. Interestingly, with increasing degree of benzolation the number of distinct features beyond this main feature decreases leading to rather broad bands at energies $\geq$ 400 eV for CuP2. For example, feature C at $\sim$ 402 eV in the spectrum of CuP0 appears as single, intense band while the spectrum of CuP2 exhibits no such isolated feature.

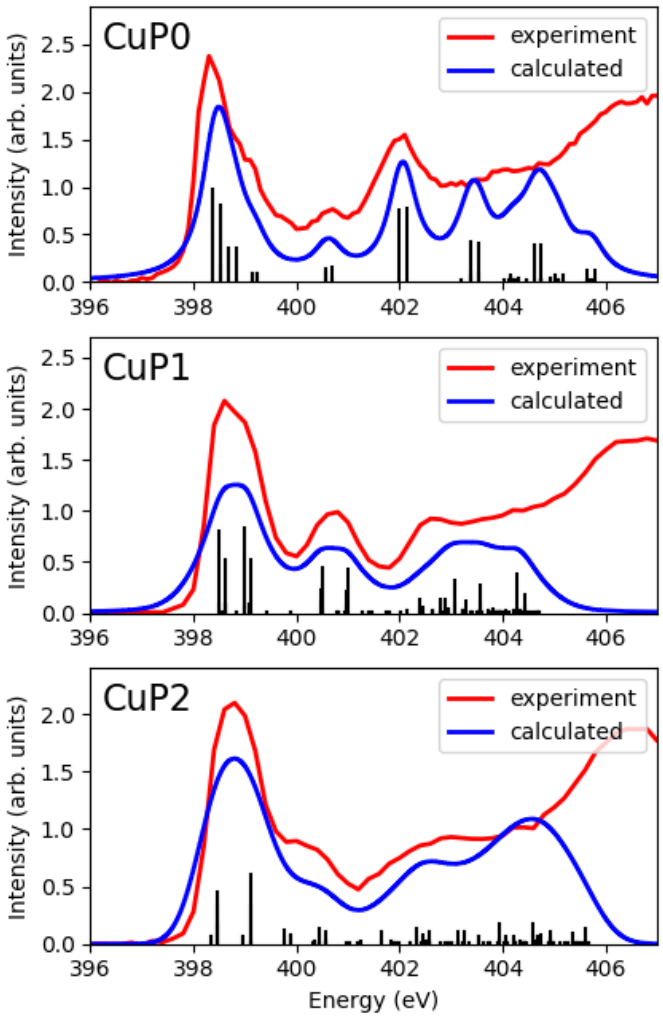

Figure 2: A comparison of experimental and calculated spectra for N K-edges. The two sets of spectra agree well up to an excitation excitation energy of $\sim$ 403 eV.

To reveal the origins of the N 1s to core excitations, the deconvoluted spectra with respect to the non-equivalent nitrogens are given in Figure 3. Herein, the blue and yellow curves correspond to the inner N_{pyr} and outer N_{aza} nitrogens, respectively. In all cases the lowest-energy main peak A has contributions from both non-equivalent nitrogens. The lowest-energy transitions for CuP0 and CuP1 correspond primarily to the outer nitrogens N_{aza}. With increasing π conjugation, transitions originating from the inner nitrogens N_{pyr} progressively shift to lower energies and higher relative intensities.

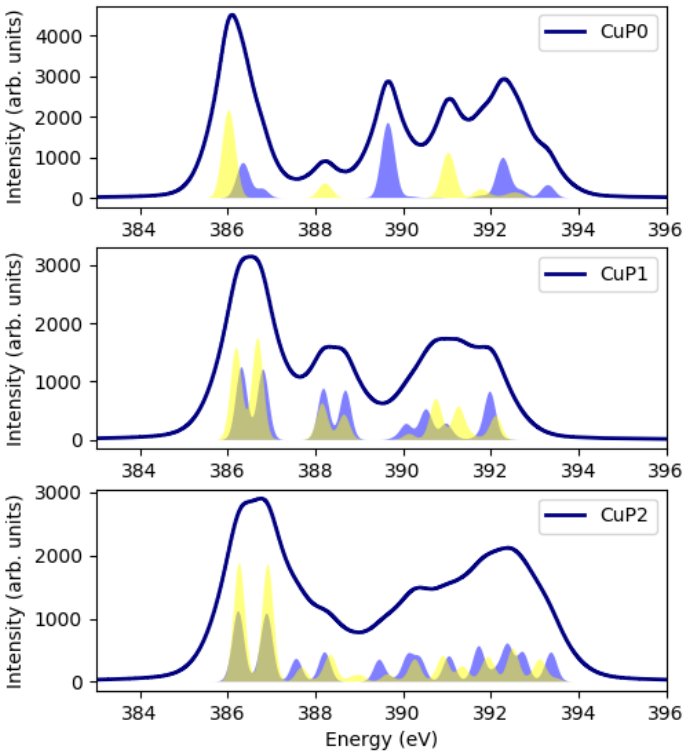

Figure 3: Deconvolution of total K-edge spectra with respect to N_{aza} (yellow) and N_{pyr} (blue).

As illustrated by their natural difference orbitals (NDO's) in Figure 4a-b the transitions corresponding to feature A in the spectrum of CuP0 have N 1s to π^* character. In contrast, the shoulder labeled A' is due to N 1s to π^* as well as N 1s to σ^* transitions (see Figure 4c-f). Finally, features B and C are dominated by N 1s to π^* transitions again (see Figure 4i-j). However, in these cases the acceptor orbitals are located more towards the periphery than for feature A. A similar trend is observed for CuP1 and CuP2 as well. While absorption bands A correspond to transitions into σ^* and π^* orbitals that are located in the vicinity of the central Cu ion, the acceptor orbitals associated with absorption bands B and C are considerably shifted towards the periphery of the molecules (see Figures 5 and 6). It should be noted that the spectrum of CuP2 at the bottom of Figure 2 is significantly broadened compared to the spectra of CuP0 and CuP1 and consequently lacks clear features. In light of our computational results this finding can be attributed to the increased number of π^* acceptor orbitals that causes a broader distribution of transitions with similar excitation

energy.

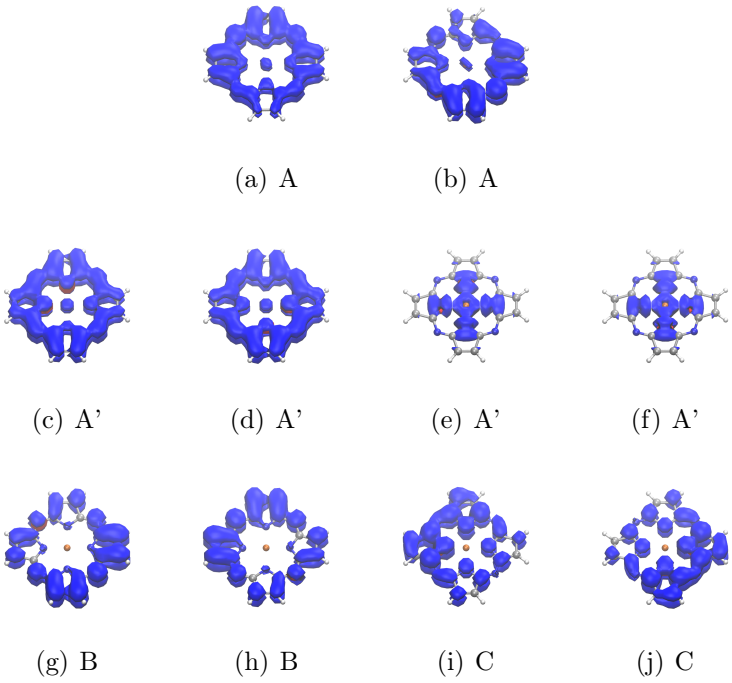

(a) A (b) A

(c) A' (d) A' (e) A' (f) A'

(g) B (h) B (i) C (j) C

Figure 4: Natural difference orbitals (NDOs) for the relevant transitions for CuP0 as labeled in Figure 2.

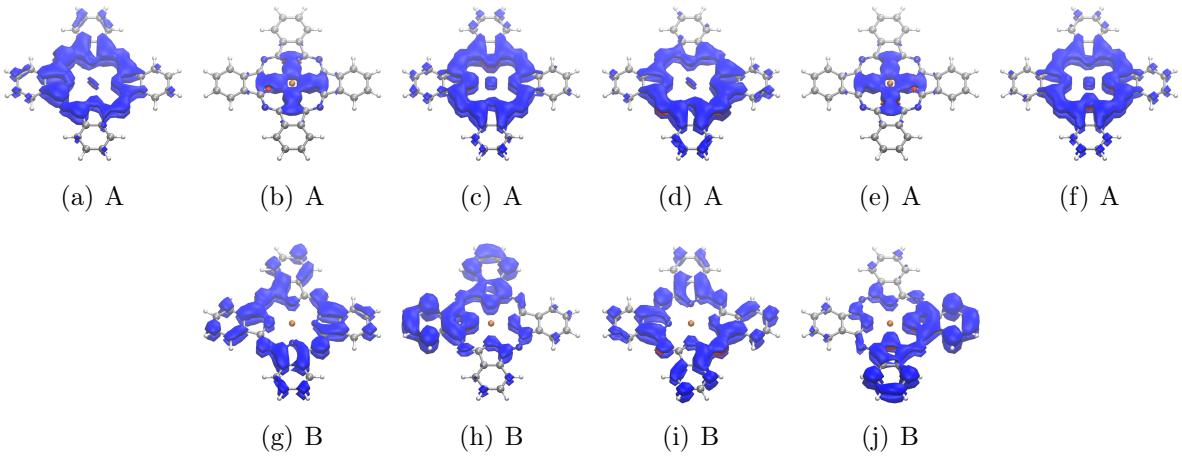

(a) A (b) A (c) A (d) A (e) A (f) A

(g) B (h) B (i) B (j) B

Figure 5: Natural difference orbitals (NDOs) for the relevant transitions for CuP1 as labeled in Figure 2.

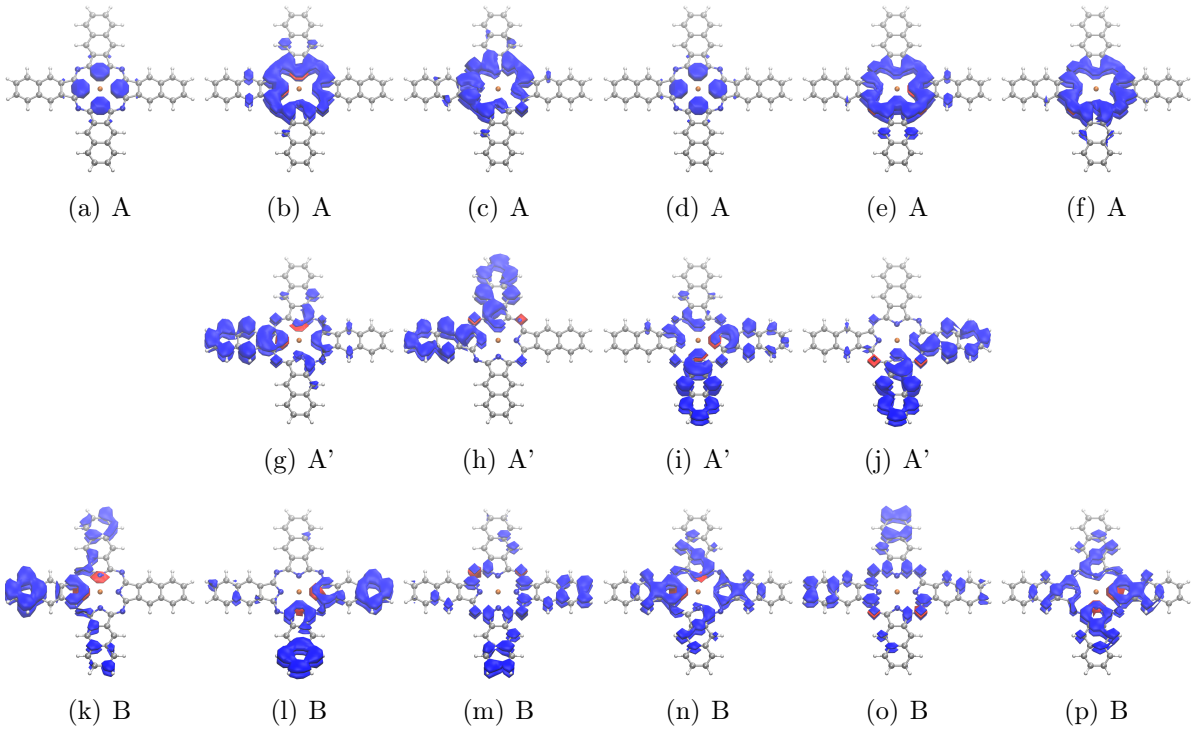

Figure 6: Natural difference orbitals (NDOs) for the relevant transitions for CuP2 as labeled in Figure 2.

Cu L-edge XAS

Experimental Spectra

The experimental L-edge spectra of CuP0 and CuP1 are shown in Figure 7 while the corresponding fitted peak positions, intensities and widths are tabulated in Table 1. We restrict the following discussion to CuP0 and CuP1 because the spectra of CuP1 and CuP2 have no visible differences (see Supporting Information) which indicates that both compounds feature similar local structural and electronic properties.

Since all dipole allowed Cu 2p to Cu 3d transitions have a $(2p^5)$ $(3d^{10})$ final state configuration the L_3- and L_2-edges exhibit only little structure. In particular the L_3- and L_2-edges of CuP1 feature only a single, sharp band. The same holds true for the L_2 edge of CuP0. Only the L_3-edge of CuP0 appears to be have a shoulder on its high-energy side, denoted as

feature B at $\sim$ 933.5 eV. Owing to its position at 1.5 eV higher than the main edge it may be due to 2p-3d transitions or be dominated by one or multiple additional MLCT transitions. A phenomenological approach to elucidate the origin of this feature is to analyze the L_3 / L_2

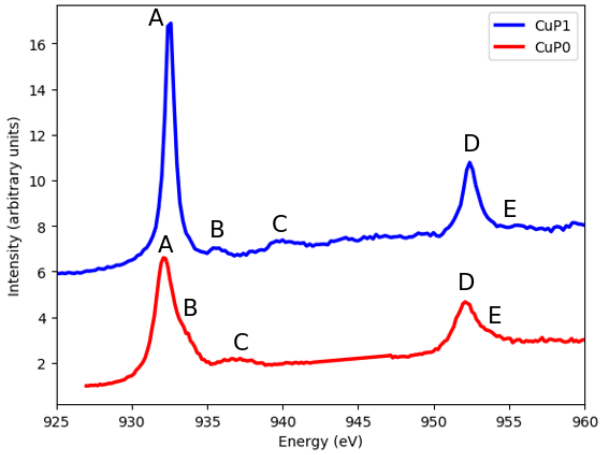

Figure 7: Experimentally observed Cu Ledge spectra of CuP0 (bottom,red) and CuP1 (top, blue).

intensity ratio. Depending on whether the shoulder is assigned to the main L_3-edge or not the intensity ratio becomes 2.41 or 1.85. A comparison to the intensity ratios of CuP1 and CuP2 (2.31 and 2.17, respectively) suggests that the shoulder is part of the main L_3-edge and thus mostly originates from 2p-3d transitions. However, application of a different peak fitting method (see Table 2 and Supporting Information) leads to a less clear picture in this regard. With the alternative fitting method the L_3 / L_2 intensity ratio amounts to 2.84 and 2.13 with or without the shoulder, respectively, while CuP1 and CuP2 exhibit values of 2.65 and 2.69, respectively. Hence a classification of feature B as originating from a 2p to 3d or a MLCT transition solely based on the experimental observations is difficult if not impossible. A further noteworthy difference between the spectra of CuP0 and CuP1 is that the main L_3-band of CuP0 is observed at a 0.43 eV lower energy than its counterpart of CuP1 (932.09 eV vs 932.52 eV). Additional weak and broad features are observed at 936.93 eV for CuP0 and at 935.69 eV and 939.89 eV for CuP1. All features beyond the L_2-edge will be omited from the discussion as this part of the experimental spectrum might be tainted from alternative decay

pathways that cannot be properly treated within the current theoretical framework. In the following, the results of quantum chemical calculations on the DFT/ROCIS and RASCI + NEVPT2 level of theory will be presented with the aim to identify the origin and character of the observed spectral features of CuP0 and CuP1.

Table 1: Fitted peak positions, intensities and widths for the experimentally observed Cu L-edges of CuP0 and CuP1 using the symmetric Voigt lineshape. All energies are given in eV.

	CuP0			**CuP1**		
Feature	**Position**	**Area**	**Width**	**Position**	**Area**	**Width**
A	932.09	10.38	1.34	932.52	13.55	0.81
B	933.20	2.47	2.01	935.69	0.50	1.75
C	936.93	0.87	2.01	939.89	1.03	1.75
D	952.11	5.40	1.61	952.43	5.90	1.09
E	953.82	6.20	2.01	955.27	2.82	1.75

Table 2: Fitted peak positions, intensities and widths for the experimentally observed Cu L-edges of CuP0 and CuP1 using an asymmetric lineshape of a gaussian convoluted Sunjic-Doniach peak. All energies are given in eV.

	CuP0			**CuP1**		
Feature	**Position**	**Area**	**Width**	**Position**	**Area**	**Width**
A	932.09	1.09	1.42	932.50	1.47	0.91
B	933.20	0.33	1.87	935.51	0.09	1.53
C	936.93	0.10	1.85	939.85	0.88	7.21
D	952.11	0.59	1.97	952.44	0.64	1.28
E	953.82	0.19	2.89	955.44	0.08	1.63

DFT/ROCIS

Figure 8 shows a comparison of the Cu L-edge spectra for CuP0 and CuP1 calculated with the DFT/ROCIS method. In agreement with the original work by Neese *et. al* the calculated transition energies have to be shifted 20.0 eV to match the experimental values.[12] Yet the main objective of this work is to elucidate the physical origin of observed transitions as well as differential transition energies and band shapes rather than to reproduce total absorption

energies.

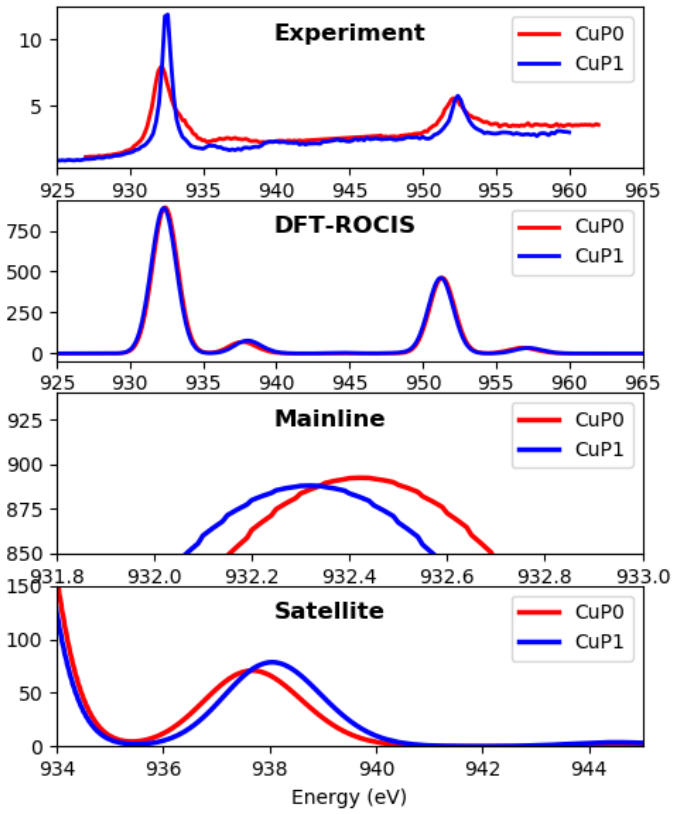

Figure 8: Experimental (top) and calculated (bottom) Cu L-edge XAS for CuP0 and CuP1 using DFT/ROCIS. Both spectra are remarkably similar with only slight energy shift of the main L_3 edge and the satellite peak. While the main absorption feature is due to 2p $\rightarrow$ $d_{x^2-y^2}$ transitions the satellite band originate from MLCT transitions. The calculated spectra were shifted by 20.0 eV.[12]

Both calculated spectra are remarkably similar as they both feature single intense L_3 and L_2 bands originating from 2p-3d transitions with no visible shoulders. In addition to the main absorption bands satellite features are predicted at 937.7 eV and 938.0 eV for CuP0 and CuP1, respectively (see Table 3). As illustrated by the orbital contour plots in the bottom panel of Figure 8 these features are dominated by transitions into two ligand π^* orbitals and a MO with mostly Cu 4s character. The second satellite feature for CuP1

at high energies is absent in the calculated spectrum and, as opposed to the experimental observations, the calculated L_3 / L_2 intensity ratio is similar for CuP0 and CuP1 with values of 1.93 and 1.92, respectively. Furthermore, no shoulder at the high energy side of the L_3-edge of CuP0 is visible in Figure 8. These results together with the absence of any low-lying MLCT states in this region indicate that the experimentally observed shoulder on the CuP0 L_3-edge arises from a splitting of the 2p to 3d manifold of states rather than a MLCT transition. Nevertheless, these results have to be considered with caution as the splitting of the states could not be reproduced and the position of the calculated satellite bands is overestimated by 0.7 eV and 2.4 eV for CuP0 and CuP1, respectively. Finally, it should be noted that a mismatch of the calculated and experimental satellite feature positions has been observed before and is to be expected with this methodology owing to its dependence on the amount of incorporated Hartree-Fock exchange in the used functional and the corresponding c_2 parameter.[12,66]

Table 3: Calculated peak positions and intensities for the Cu L-edges of CuP0 and CuP1. All energies are given in eV.

	CuP0		**CuP1**	
Feature	**Position**	**Intensity**	**Position**	**Intensity**
L_3	932.42	892.4	932.32	888.0
L_3 satellite	937.67	70.8	938.04	78.6
L_2	951.34	462.4	951.23	462.1
L_2 satellite	956.81	35.1	957.21	33.5

Restricted Active Space Approach

Active Space selection Since the valence orbital space of the systems explored in the current study are composed of a large number of ligand-based π orbitals, the active space selection and the treatment of core-excited state multiplets are far from being trivial. Calculating a wealth of complete multiplets (doublet-doublet as well as doublet-quartet type excitations) in the presence of dynamic electron correlation, while maintaining a large va-

lence active space that can capture all the essential information regarding the corresponding electronic structure unsurprisingly gives rise to an exhaustive computational cost. Therefore the aforementioned restricted active space CI approach together with second order n-electron valence perturbation theory to describe electron correlation (RASCI+NEVPT2) was used in combination with the recently introduced Active Space Selection based on 1st order perturbation theory (ASS1ST)[1] scheme to chose active spaces that include all strongly correlated orbitals but are as small possible.[53] In a nutshell, ASS1ST produces a set of quasi-restricted natural orbitals for the internal and external orbital space, respectively. Based on the corresponding natural orbital occupation numbers (NOONs) the correlation strength of the natural orbitals is estimated which in turn serves as basis for the inclusion (or exclusion) of the natural orbitals in the active space. The starting point for the ASS1ST procedure in the current cases was an active space of 9 electrons in 5 orbitals reflecting the Cu (3d^9) configuration. As depicted in Figure 9 two additional internal and external orbitals of CuP0

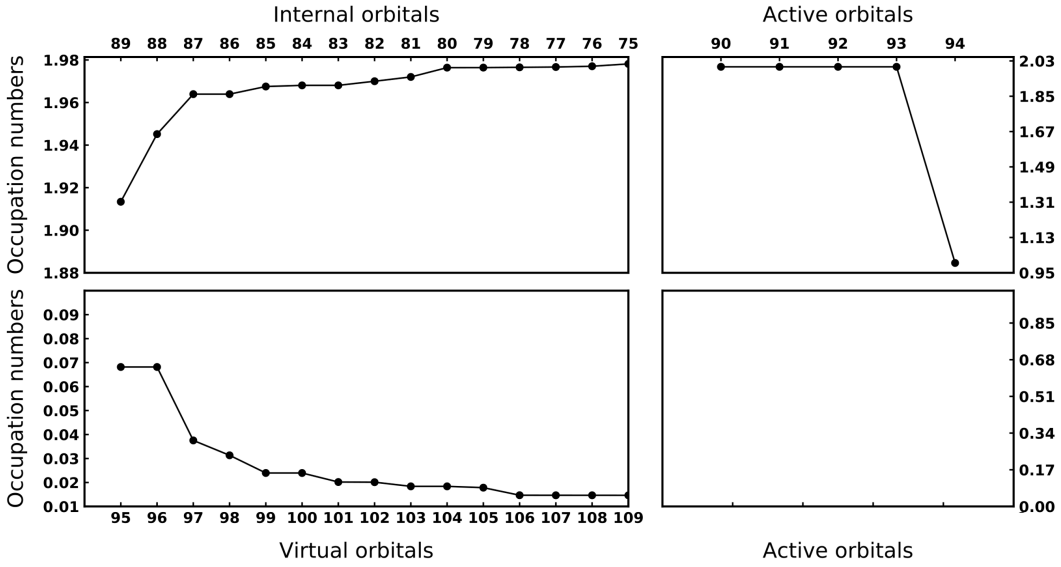

Figure 9: Natural orbital occupation number (NOON) distribution obtained from ASS1ST for CuP0. The corresponding NOON distribution for CuP1 can be found in the Supporting Information.

[1]The ASS1ST calculations presented in this work already applied a yet unpublished feature that greatly speeds up the calculations at a minimal loss of conceptual rigor. The corresponding manuscript was recently submitted for publication.

are strongly correlated with occupation numbers of ~ 1.92, ~ 1.94 and ~ 0.07, respectively. As expected for extended conjugated π systems multiple further orbitals feature occupation numbers that considerably differ from both 0.0 and 2.0. However, owing to the aforementioned computational restrictions only orbitals with a non-negligible contribution from Cu orbitals were included resulting in a (7,7) active space. After a state-averaged optimization of all molecular orbitals with respect to all excited states up to 12 eV as recommended previously[25] the active orbitals took the form displayed in Figure 10. They comprise the singly occupied orbital with mostly Cu $3d_{x^2-y^2}$ character and its bonding counterpart together with a pair of bonding and antibonding ligand π-orbitals and the Cu 4s orbital. Analogous active orbitals were obtained for CuP1 (see Supporting Information).

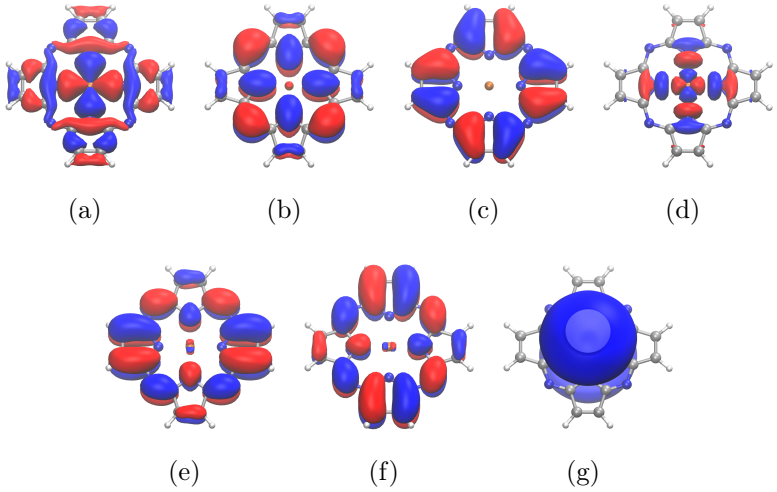

Figure 10: Optimized active orbitals for CuP0.

RASCI + NEVPT2 Figure 11 shows the calculated Cu L-edge spectra for CuP0 and CuP1 at the RASCI(13,10) and RASCI(13,10) + NEVPT2 levels of theory. Note, that these active spaces incorporate the above discussed valence active orbitals and the Cu 2p-orbitals in order to enable the calculation of the desired core excited states. Analogous to the DFT/ROCIS results (see above) the calculated spectra have to be shifted by -11.2 eV and 7.0 eV, respectively, to match the experimentally observed transition energies. As expected, the calculated spectra for CuP0 and CuP1 exhibit great similarities. More precisely, both spectra

feature single intense L_3 and L_2 bands with no visible shoulders and similar L_3 / L_2 intensity ratios of 1.97 (CuP0) and 1.98 (CuP1). Hence, the RASCI(13,10) + NEVPT2 results neither reproduce the experimentally observed shoulder on the high energy side of the L_3-edge of CuP0 nor its shift of 0.4 eV relative to the L_3-edge of CuP1. The only considerable difference

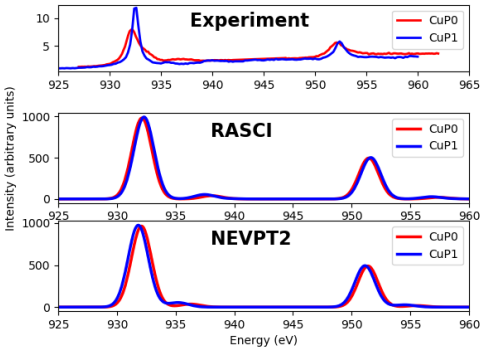

Figure 11: Experimental (top) and calculated (bottom) Copper L-edge XAS for Copper porphyrazine P0 and phthalocyanine P1 using RASCI(7,7) (top) and RASCI(7,7)+NEVPT2 protocol.

between the two calculated spectra is the position of the satellite feature on the high energy side of the main L_3 edge. While it is predicted at 936.7 eV for CuP0 it occurs at 935.6 eV for CuP1 (see Table 4). In both cases the position of the satellite features agrees remarkably well with the experimental spectra with deviations on the order of 0.2 eV. We thus conclude that the chosen active space is well suited for the problem at hand. Nevertheless, it is important to note that a treatment of dynamic electron correlation on top of the RASCI calculation is imperative to obtain this level of accuracy since the same features are considerably shifted to higher energies ($\sim$ 2eV) at the RASCI level of theory (see Table 4). In agreement with our DFT/ROCIS results, our RASCI(13,10) + NEVPT2 calculations indicate that the satellite features originate mostly from 2p $\rightarrow \pi^*$ transitions for both, CuP0 and CuP1 (Figure 10). In a simple orbital energy based picture the considerable shift of the peak position towards a lower transition energy by $\sim$ 1 eV for CuP1 might thus be associated with a lowering of the π^* acceptor orbital energies on account of the enlargement of the conjugated π-system. Of course, if the active space does not include any ligand-centered π (and π^*) orbitals but

only metal-centered 3d-orbitals none of the satellite features could possibly be predicted by the RASCI or RASCI + NEVPT2 calculations at all. Following this line of argument the absence of the second satellite band for CuP1 in the calculated spectrum is probably due to the limited number of ligand-centered active orbitals. However, considering the steep increase in computational cost with growing number of active orbitals and the potentially large number of required orbitals to reproduce this feature we refrain from increasing the active space size beyond this point.

Table 4: Calculated peak positions and intensities for the Cu L-edges of CuP0 and CuP1 at the RASCI(13,10) and RASCI(13,10) + NEVPT2 level of theory. All energies are given in eV.

	CuP0		**CuP1**	
Feature	**Position**	**Intensity**	**Position**	**Intensity**
RASCI L_3	932.2	980.3	932.4	992.6
RASCI L_3 satellite	938.2	39.4	937.5	54.2
NEVPT2 L_3	932.5	963.2	932.2	973.8
NEVPT2 L_3 satellite	936.7	37.0	935.6	55.1

Summary and Conclusions

This work contains an analysis of the experimentally observed N K-edge and Cu L-edge of three Cu porphyrazine derivatives labeled CuP0, CuP1 and CuP2 based on electronic structure calculations. According to our (and previous) calculations the electronic ground state of all three porphyrazines is dominated by a Cu ($3d^9$) configuration with a singly occupied $3d_{x^2-y^2}$ orbitals as is expected for square-planar Cu^{II} compounds.

For N K-edge spectra remarkable agreement between calculated and experimental spectra was found in the investigated spectral region of up to 5-6 eV above the rising edge. The first and most intense spectral feature A of that region originates from multiple transitions into low-lying π^* and σ^* transitions. Interestingly, the progressive broadening of the feature can be connected to a redistribution of contributions from the symmetrically inequivalent

sets of N_{aza} and N_{pyr} atoms. Higher energy features B through D all correspond to N 1 $\rightarrow \pi^*$ transitions. With increasing degree of benzolation the larger number of available π^* orbitals leads to a general broadening of these features. A general trend for features B through D is that the higher the transition energy the more the excited electron is located towards the periphery of the molecule.

Owing to the $(2p^5)$ $(3d^{10})$ final state configuration of the corresponding excited states the experimental Cu L-edge spectra of CuP0, CuP1 and CuP2 exhibit only little structure. Besides the main edge peaks only a weakly resolved shoulder at the high energy side of the L_3 edge of CuP0 and satellite features between the L_3 and L_2 edges are observed. From an experimental point of view the origin of the shoulder is somewhat unclear. Interestingly, neither our DFT/ROCIS nor our RASCI + NEVPT2 calculations can reproduce the shoulder for CuP0. It may thus be inferred that it is due to effects that are outside of the current models, e.g. axial ligation, interactions with the surface or other porphyrazines etc. Nevertheless, the absence of any intense metal-to-ligand charge-transfer bands in this region of the calculated spectra indicates that the shoulder rather originates from a splitting of the main L_3 edge than from additional MLCT bands. Both theoretical approaches connect the satellite bands at 936.9 eV and 935.7 eV for CuP0 and CuP1, respectively, to transitions into low-lying π^* orbitals. Accordingly the observed energetical shift can be connected to an energetic lowering of the acceptor orbitals due to the extension of the conjugated π system. From a technical point of view it should be noted that while the DFT/ROCIS method fails to give accurate transition energies for the satellite bands owing to its inherent dependence on the empirical c_2 parameter the RASCI + SC-NEVPT2 results are in good agreement with the experimental values. Importantly, the treatment of dynamic electron correlation effects and the inclusion of ligand-centered orbitals in the active space are prerequisites for achieving this level of qualitative and quantitative accuracy.

Acknowledgement

The authors thank the Deutsche Forschungsgemeinschaft (DFG) for funding through Emmy-Noether project RO 5688/1-1.

References

(1) Golnak, R.; Bokarev, S. I.; Seidel, R.; Xiao, J.; Grell, G.; Atak, K.; Unger, I.; Thürmer, S.; Aziz, S. G.; Kühn, O.; Winter, B.; Aziz, E. F. Joint analysis of radiative and non-radiative electronic relaxation upon X-ray irradiation of transition metal aqueous solutions. *Scientific reports* **2016**, *6*, 1–8.

(2) Glaser, T.; Hedman, B.; Hodgson, K.; Solomon, E. Ligand K-edge X-ray absorption spectroscopy: a direct probe of ligand-metal covalency. *Acc. Chem. Res.* **2000**, *33*, 859–868.

(3) Sarangi, R.; DeBeer George, S.; Rudd, D. J.; Szilagyi, R. K.; Ribas, X.; Rovira, C.; Almeida, M.; Hodgson, K. O.; Hedman, B.; Solomon, E. I. Sulfur k-edge x-ray absorption spectroscopy as a probe of ligand- metal bond covalency: metal vs ligand oxidation in copper and nickel dithiolene complexes. *J. Am. Chem. Soc.* **2007**, *129*, 2316–2326.

(4) Lee, K.; Wei, H.; Blake, A. V.; Donahue, C. M.; Keith, J. M.; Daly, S. R. Ligand K-edge XAS, DFT, and TDDFT analysis of pincer linker variations in Rh (I) PNP complexes: reactivity insights from electronic structure. *Dalton Trans.* **2016**, *45*, 9774–9785.

(5) DeBeer, S.; Petrenko, T.; Neese, F. Time-Dependent Density Functional Calculations of Ligand K-edge X-ray Absorption Spectra. *Inorg. Chim. Acta* **2008**, *361*, 965–972.

(6) Thole, B. T.; van der Laan, G. Branching ratio in x-ray absorption spectroscopy. *Phys. Rev. B* **1988**, *38*, 3158.

(7) de Groot, F. M. F.; Fuggle, J. C.; Thole, B. T.; Sawatzky, G. A. 2p x-ray absorption of 3d transition-metal compounds: An atomic multiplet description including the crystal field. *Phys. Rev. B* **1990**, *42*, 5459.

(8) Bagus, P.; Freund, H.; Kuhlenbeck, H.; Ilton, E. A new analysis of X-ray adsorption branching ratios: Use of Russell-Saunders coupling. *Chem. Phys. Lett.* **2008**, *455*, 331–334.

(9) Stavitski, E.; de Groot, F. The CTM4XAS program for EELS and XAS spectral shape analysis of transition metal L edges. *Micron* **2010**, *41*, 687–694.

(10) Ikeno, H.; Mizoguchi, T.; Tanaka, I. Ab initio charge transfer multiplet calculations on the $L_{2,3}$ XANES and ELNES of 3d transition metal oxides. *Phys. Rev. B* **2011**, *83*, 155107.

(11) Haverkort, M.; Zwierzycki, M.; Andersen, O. Multiplet ligand-field theory using Wannier orbitals. *Phys. Rev. B* **2012**, *85*, 165113.

(12) Roemelt, M.; Maganas, D.; DeBeer, S.; Neese, F. A combined DFT and restricted open-shell configuration interaction method including spin-orbit coupling: Application to transition metal L-edge X-ray absorption spectroscopy. *J. Chem. Phys.* **2013**, *138*, 204101.

(13) Maganas, D.; Roemelt, M.; Hävecker, M.; Trunschke, A.; Knop-Gericke, A.; Schlögl, R.; Neese, F. First principles calculations of the structure and V L-edge X-ray absorption spectra of V2O5 using local pair natural orbital coupled cluster theory and spin-orbit coupled configuration interaction approaches. *Phys. Chem. Chem. Phys.* **2013**, *15*, 7260–7276.

(14) Maganas, D.; Roemelt, M.; Weyhermüller, T.; Blume, R.; Hävecker, M.; Knop-Gericke, A.; DeBeer, S.; Schlögl, R.; Neese, F. L-edge X-ray absorption study of

mononuclear vanadium complexes and spectral predictions using a restricted open shell configuration interaction ansatz. *Phys. Chem. Chem. Phys.* **2014**, *16*, 264–276.

(15) Maganas, D.; DeBeer, S.; Neese, F. Restricted open-shell configuration interaction cluster calculations of the L-edge x-ray absorption study of TiO2 and CaF2 solids. *Inorg. Chem.* **2014**, *53*, 6374–6385.

(16) Atak, K.; Golnak, R.; Xiao, J.; Pflüger, M.; Brandenburg, T.; Winter, B.; Aziz, E. F. Co (III) protoporphyrin IX chloride in solution: spin-state and metal coordination revealed from resonant inelastic X-ray scattering and electronic structure calculations. *Phys. Chem. Chem. Phys.* **2015**, *17*, 3409–3414.

(17) Lalithambika, S. S. N.; Atak, K.; Seidel, R.; Neubauer, A.; Brandenburg, T.; Xiao, J.; Winter, B.; Aziz, E. F. Chemical bonding in aqueous hexacyano cobaltate from photon- and electron-detection perspectives. *Scientific reports* **2017**, *7*, 1–13.

(18) Sreekantan Nair Lalithambika, S.; Golnak, R.; Winter, B.; Atak, K. Electronic Structure of Aqueous [Co (bpy) 3] 2+/3+ Electron Mediators. *Inorg. Chem.* **2019**, *58*, 4731–4740.

(19) Josefsson, I.; Kunnus, K.; Schreck, S.; Föhlisch, A.; de Groot, F. M. F.; Wernet, P.; Odelius, M. Ab Initio Calculations of X-ray Spectra: Atomic Multiplet and Molecular Orbital Effects in a Multiconfigurational SCF Approach to the L-Edge Spectra of Transition Metal Complexes. *J. Phys. Chem. Lett.* **2012**, *3*, 3565–3570.

(20) Bokarev, S. I.; Dantz, M.; Suljoti, E.; Kühn, O.; Aziz, E. F. State-dependent electron delocalization dynamics at the solute-solvent interface: soft-x-ray absorption spectroscopy and Ab initio calculations. *Phys. Rev. Lett.* **2013**, *111*, 083002.

(21) Pinjari, R. V.; Delcey, M. G.; Guo, M.; Odelius, M.; Lundberg, M. Restricted active space calculations of L-edge X-ray absorption spectra: From molecular orbitals to multiplet states. *J. Chem. Phys.* **2014**, *141*, 124116.

(22) Preuße, M.; Bokarev, S. I.; Aziz, S. G.; Kühn, O. Towards an ab initio theory for metal L-edge soft X-ray spectroscopy of molecular aggregates. *Struct. Dyn.* **2016**, *3*, 062601.

(23) Pinjari, R. V.; Delcey, M. G.; Guo, M.; Odelius, M.; Lundberg, M. Cost and sensitivity of restricted active-space calculations of metal L-edge X-ray absorption spectra. *J. Comp. Chem.* **2016**, *37*, 477–486.

(24) Guo, M.; Källman, E.; Pinjari, R. V.; Couto, R. C.; Kragh Sørensen, L.; Lindh, R.; Pierloot, K.; Lundberg, M. Fingerprinting electronic structure of heme iron by ab initio modeling of metal L-edge X-ray absorption spectra. *J. Chem. Theory Comput.* **2018**, *15*, 477–489.

(25) Chantzis, A.; Kowalska, J. K.; Maganas, D.; DeBeer, S.; Neese, F. Ab Initio Wave Function-Based Determination of Element Specific Shifts for the Efficient Calculation of X-ray Absorption Spectra of Main Group Elements and First Row Transition Metals. *J. Chem. Theory Comput.* **2018**, *14*, 3686–3702.

(26) Maganas, D.; Kowalska, J. K.; Nooijen, M.; DeBeer, S.; Neese, F. Comparison of multireference ab initio wavefunction methodologies for X-ray absorption edges: A case study on [Fe(II/III)Cl4]2-/1- molecules. *J. Chem. Phys.* **2019**, *150*, 104106.

(27) Bokarev, S. I.; Kühn, O. Theoretical X-ray spectroscopy of transition metal compounds. *WIREs Comp. Mol. Sci.* **2020**, *10*, e1433.

(28) Pop, D.; Winter, B.; Freyer, W.; Weber, R.; Widdra, W.; Hertel, I. V. Photoelectron Spectroscopy on Thin Films of Extended Copper Porphyrazines. *J. Phys. Chem. B* **2004**, *108*, 9158–9167.

(29) De La Torre, G.; Vazquez, P.; Agullo-Lopez, F.; Torres, T. Role of structural factors in the nonlinear optical properties of phthalocyanines and related compounds. *Chem. Rev.* **2004**, *104*, 3723–3750.

(30) Sorokin, A. B. Phthalocyanine metal complexes in catalysis. *Chem. Rev.* **2013**, *113*, 8152–8191.

(31) Martín-Gomis, L.; Fernández-Lázaro, F.; Sastre-Santos, Á. Advances in phthalocyanine-sensitized solar cells (PcSSCs). *J. Mater. Chem. A* **2014**, *2*, 15672–15682.

(32) Lo, P.-C.; Rodríguez-Morgade, M. S.; Pandey, R. K.; Ng, D. K.; Torres, T.; Dumoulin, F. The unique features and promises of phthalocyanines as advanced photosensitisers for photodynamic therapy of cancer. *Chem. Soc. Rev.* **2020**,

(33) Batchelor, D.; Pop, D.; Winters, B.; Freyer, W.; Sperling, M.; Tepper, B.; Widdra, W. NEXAFS study of a family of Copper Porphyrazines. *BESSY – Annual Report 2002* **2002**,

(34) Pop, D. Photoelectron Spectroscopy on Thin Films of Cu-, Zn-, and Metal-Free Extended Porphyrazines. Ph.D. thesis, Freie Universität Berlin, 2003.

(35) Batchelor, D. R.; Follath, R.; Schmeißer, D. Commissioning Results of the BTUC-PGM beamline. *Nucl. Instrum. Methods Phys. Res., Sect. A* **2001**, *467*, 470–473.

(36) Fuchs, O. Soft x-ray spectroscopy of organic molecules and liquids. Ph.D. thesis, Universität Würzburg, Fakultät für Physik und Astronomie, 2009.

(37) Neese, F. Software update: the ORCA program system, version 4.0. *WIREs Comp. Mol. Sci.* **2018**, *8*, e1327.

(38) Becke, A. A New Mixing of Hartree-Fock and Local Density-Functional Theories. *J. Chem. Phys.* **1993**, *98*, 1372.

(39) Becke, A. D. Density-Functional Thermochemistry. 3. The Role of Exact Exchange. *J. Chem. Phys.* **1993**, *98*, 5648–5652.

(40) Weigend, F.; Ahlrichs, R. Balanced Basis Sets of Split Valence, Triple Zeta Valence and Quadruple Zeta Valence Quality for H to Rn: Design and Assessment of Accuracy. *Phys. Chem. Chem. Phys.* **2005**, *7*, 3297–3305.

(41) Neese, F.; Wennmohs, F.; Hansen, A.; Becker, U. Efficient, Approximate and Parallel Hartree-Fock and Hybrid DFT Calculations. A 'Chain-of-Spheres' Algorithm for the Hartree-Fock Exchange. *Chem. Phys.* **2009**, *356*, 98–109.

(42) Dunlap, B. I.; Connolly, J. W. D.; Sabin, J. R. Some Approximations in Applications of X-Alpha Theory. *J. Chem. Phys.* **1979**, *71*, 3396–3402.

(43) Vahtras, O.; Almlöf, J.; Feyereisen, M. W. Integral Approximations for LCAO-SCF Calculations. *Chem. Phys. Lett.* **1993**, *213*, 514–518.

(44) Neese, F. An improvement of the resolution of the identity approximation for the formation of the Coulomb matrix. *J. Comput. Chem.* **2003**, *24*, 1740–1747.

(45) Weigend, F. Accurate Coulomb-Fitting Basis Sets for H to Rn. *Phys. Chem. Chem. Phys.* **2006**, *8*, 1057–1065.

(46) Runge, E.; Gross, E. Density-Functional Theory for Time-Dependent Systems. *Phys. Rev. Lett.* **1984**, *52*, 997–1000.

(47) Pipek, J.; Mezey, P. G. A fast intrinsic localization procedure applicable for abinitio and semiempirical linear combination of atomic orbital wave functions. *J. Chem. Phys.* **1989**, *90*, 4916–4926.

(48) Hirata, S.; Head-Gordon, M. Time-Dependent Density Functional Theory within the Tamm-Dancoff Approximation. *Chem. Phys. Lett.* **1999**, *314*, 291–299.

(49) Lenthe, E. v.; Baerends, E. J.; Snijders, J. G. Relativistic Regular Two-Component Hamiltonians. *J. Chem. Phys.* **1993**, *99*, 4597–4610.

(50) van Wüllen, C. Molecular Density Functional Calculations in the Regular Relativistic Approximation: Method, Application to Coinage Metal Diatomics, Hydrides, Fluorides and Chlorides, and Comparison with First-Order Relativistic Calculations. *J. Chem. Phys.* **1998**, *109*, 392.

(51) DeBeer George, S.; Petrenko, T.; Neese, F. Prediction of Iron K-Edge Absorption Spectra Using Time-Dependent Density Functional Theory. *J. Phys. Chem. A* **2008**, *112*, 12936–12943.

(52) Roemelt, M.; Krewald, V.; Pantazis, D. A. Exchange Coupling Interactions from the Density Matrix Renormalization Group and N-Electron Valence Perturbation Theory: Application to a Biomimetic Mixed-Valence Manganese Complex. *J. Chem. Theory Comput.* **2018**, *14*, 166–179.

(53) Khedkar, A.; Roemelt, M. Active Space Selection Based on Natural Orbital Occupation Numbers from n-Electron Valence Perturbation Theory. *J. Chem. Theory Comput.* **2019**, *15*, 3522–3536.

(54) Angeli, C.; Cimiraglia, R.; Evangelisti, S.; Leininger, T.; Malrieu, J. Introduction of n-electron valence states for multireference perturbation theory. *J. Chem. Phys.* **2001**, *114*, 10252.

(55) Angeli, C.; Cimiraglia, R.; Malrieu, J. n-electron valence state perturbation theory: A spinless formulation and an efficient implementation of the strongly contracted and of the partially contracted variants. *J. Chem. Phys.* **2002**, *117*, 9138.

(56) Hess, B. A.; Marian, C. M.; Wahlgren, U.; Gropen, O. A mean-field spin-orbit method applicable to correlated wavefunctions. *Chem. Phys. Lett.* **1996**, *251*, 365–371.

(57) Douglas, M.; Kroll, N. M. Quantum electrodynamical corrections to the fine structure of helium. *Annals of Physics* **1974**, *82*, 89–155.

(58) Hess, B. A. Relativistic electronic-structure calculations employing a two-component no-pair formalism with external-field projection operators. *Phys. Rev. A* **1986**, *33*, 3742–3748.

(59) De Jong, W. A.; Harrison, R. J.; Dixon, D. A. Parallel Douglas–Kroll energy and gradients in NWChem: estimating scalar relativistic effects using Douglas–Kroll contracted basis sets. *J. Chem. Phys.* **2001**, *114*, 48–53.

(60) Balabanov, N. B.; Peterson, K. A. Systematically convergent basis sets for transition metals. I. All-electron correlation consistent basis sets for the 3d elements Sc–Zn. *J. Chem. Phys.* **2005**, *123*, 064107.

(61) Balabanov, N. B.; Peterson, K. A. Basis set limit electronic excitation energies, ionization potentials, and electron affinities for the 3d transition metal atoms: Coupled cluster and multireference methods. *J. Chem. Phys.* **2006**, *125*, 074110.

(62) Stoychev, G. L.; Auer, A. A.; Neese, F. Automatic generation of auxiliary basis sets. *J. Chem. Theory Comput.* **2017**, *13*, 554–562.

(63) De Francesco, R.; Stener, M.; Fronzoni, G. Theoretical Study of Near-Edge X-ray Absorption Fine Structure Spectra of Metal Phthalocyanines at C and N K-Edges. *J. Phys. Chem. A* **2012**, *116*, 2885–2894.

(64) Wallace, A. J.; Williamson, B. E.; Crittenden, D. L. CASSCF-based explicit ligand field models clarify the ground state electronic structures of transition metal phthalocyanines (MPc; M = Mn, Fe, Co, Ni, Cu, Zn). *Can. J. Chem.* **2016**, *94*, 1163–1168.

(65) Gouterman, M. Spectra of Porphyrins. *J. Mol. Spectrosc.* **1961**, *6*, 138–163.

(66) Roemelt, M.; Beckwith, M. A.; Duboc, C.; Collomb, M.-N.; Neese, F.; DeBeer, S. Manganese K-Edge X-Ray Absorption Spectroscopy as a Probe of the Metal-Ligand Interactions in Coordination Compounds. *Inorg. Chem.* **2012**, *51*, 680–687.

Graphical TOC Entry